AMERICAN SOCIETY FOR MICROBIOLOGY | Journal of Virology®

GENOME REPLICATION AND REGULATION OF VIRAL GENE EXPRESSION

Proteolytic Processing of the Coronavirus Replicase Nonstructural Protein 14 Exonuclease Is Not Required for Virus Replication but Alters RNA Synthesis and Viral Fitness

Jordan Anderson-Daniels,[a] Jennifer Gribble,[b]* Mark Denison[a,b,c]

[a]Department of Pediatrics, Vanderbilt University Medical Center, Nashville, Tennessee, USA
[b]Department of Pathology, Microbiology, and Immunology, Vanderbilt University Medical Center, Nashville, Tennessee, USA
[c]Vanderbilt Institute for Infection, Immunology, and Inflammation, Nashville, Tennessee, USA

ABSTRACT Coronaviruses (CoVs) initiate replication by translation of the positive-sense RNA genome into the replicase polyproteins connecting 16 nonstructural protein domains (nsp1-16), which are subsequently processed by viral proteases to yield mature nsp. For the betacoronavirus murine hepatitis virus (MHV), total inhibition of translation or proteolytic processing of replicase polyproteins results in rapid cessation of RNA synthesis. The nsp5-3CLpro (Mpro) processes nsps7-16, which assemble into functional replication-transcription complexes (RTCs), including the enzymatic nsp12-RdRp and nsp14-exoribonuclease (ExoN)/N7-methyltransferase. The nsp14-ExoN activity mediates RNA-dependent RNA proofreading, high-fidelity RNA synthesis, and replication. To date, the solved partial RTC structures, biochemistry, and models use or assume completely processed, mature nsp. Here, we demonstrate that in MHV, engineered deletion of the cleavage sites between nsp13-14 and nsp14-15 allowed recovery of replication-competent virus. Compared to wild-type (WT) MHV, the nsp13-14 and nsp14-15 cleavage deletion mutants demonstrated delayed replication kinetics, impaired genome production, altered abundance and patterns of recombination, and impaired competitive fitness. Further, the nsp13-14 and nsp14-15 mutant viruses demonstrated mutation frequencies that were significantly higher than with the WT. The results demonstrate that cleavage of nsp13-14 or nsp14-15 is not required for MHV viability and that functions of the RTC/nsp14-ExoN are impaired when assembled with noncleaved intermediates. These data will inform future genetic, structural, biochemical, and modeling studies of coronavirus RTCs and nsp 13, 14, and 15 and may reveal new approaches for inhibition or attenuation of CoV infection.

IMPORTANCE Coronavirus replication requires proteolytic maturation of the nonstructural replicase proteins to form the replication-transcription complex. Coronavirus replication-transcription complex models assume mature subunits; however, mechanisms of coronavirus maturation and replicase complex formation have yet to be defined. Here, we show that for the coronavirus murine hepatitis virus, cleavage between the nonstructural replicase proteins nsp13-14 and nsp14-15 is not required for replication but does alter RNA synthesis and recombination. These results shed new light on the requirements for coronavirus maturation and replication-transcription complex assembly, and they may reveal novel therapeutic targets and strategies for attenuation.

KEYWORDS coronavirus, exonuclease, maturation, protease cleavage, replication-transcription complex

Positive-strand RNA viruses initiate replication by host-mediated translation of genome +RNA into protein. A limitation of this strategy is the lack of protein diversity that can be translated from a single mRNA. Positive-strand RNA viruses have evolved

Editor Tom Gallagher, Loyola University Chicago

Copyright © 2022 American Society for Microbiology. All Rights Reserved.

Address correspondence to Mark Denison, mark.denison@vumc.org.

*Present address: Jennifer Gribble, Integrated DNA Technologies, Coralville, Iowa, USA.

The authors declare no conflict of interest.

Received 26 May 2022
Accepted 13 July 2022
Published 4 August 2022

around this limitation by coding for polyproteins and/or ribosomal frameshifting to maximize the genetic potential of a single RNA molecule (1–6). However, this requires the use of viral or host proteases to process the polyproteins into the mature proteins (7). Inhibition of polyprotein processing is often lethal to viral replication, and as such, viral proteases are targets for therapeutic intervention (8–11).

Coronaviruses (CoVs) have the largest-known RNA genomes, ranging from 27 to 32 kb. The first two-thirds of the genome code for 16 nonstructural proteins, nsps1-16, while the 3′ end of the genome codes for structural and accessory proteins (12, 13). Two open reading frames at the 5′ end of the genome (ORF1a and ORF1ab) drive expression of the nonstructural proteins as two co-amino-terminal polyproteins, pp1a and pp1ab. ORF1a translation results in nsp1-10 expression, and a ribosomal frameshift in nsp12 results in ORF1ab, consisting of nsp1-16 (Fig. 1A) (2–6). Proteolytic processing of the 16 nonstructural proteins is mediated by two or three virus-encoded proteinases, depending on the CoV subgenera and species. These include one or two papain-like proteases (PLpro) in nsp3 and one 3C-like protease in nsp5 (Mpro), henceforth referred to as nsp5 (7). The nsp5 processes the pp1a and pp1ab polyproteins from nsp4-16 (Fig. 1A). Coronavirus cleavage site motifs consist of 10 amino acids designated P5-P1/P1′-P5′, where polyprotein subunits are cleaved between the P1/P1′ residues (Fig. 1B). While the 11 nsp5 P5-P5′ cleavage motifs are unique between each subunit, the P1 cleavage residue is a conserved Gln at every known CoV nsp5 cleavage site (Fig. 1B), with the single exception in HCoV-HKU1 between nsp13-14, which encodes a His residue (14–22). All biochemical and virological experiments indicate that deletion of the P1 Gln prevents nsp5-driven cleavage (23–25).

CoV RNA synthesis is mediated by the replication-transcription complex (RTC) involving nsps7-16. nsps7-10 are nonenzymatic cofactors that bind and facilitate the enzymatic activities of nsps12-16 (26–37). nsp12 contains RNA-dependent RNA polymerase and nucleotidyltransferase activities responsible for genome replication and subgenomic production, which are facilitated through binding of nsps 7 and 8 (29, 32, 38–42). nsp14 is also a multidomain protein linking a 3′-5′ exoribonuclease, which regulates replication fidelity, recombination, and immune evasion, and an N-7 methyltransferase that is required for genome capping and immune evasion. The nsp14 ExoN activity is either enhanced by or requires interaction with the nonenzymatic nsp10 (35, 37, 43–57). Genome capping also involves the activity of the nsp16 2'-O-methyltransferase, bound to nsp10 (34, 58). The adjacent nsp13 helicase/nucleoside triphosphatase (59–62) and nsp15 uridylate-specific endoribonuclease (63, 64) also function during replication, and their contributions to the RTC and replication are active areas of investigation. All current models of the coronavirus RTC present proteins as mature, proteolytically processed forms of nsps7-16. While some studies have investigated the requirement for cleavage between nsps7-12 (23, 24), there are currently no reports on the requirements for cleavage between the enzymatic components of the RTC (nsps12-16). Thus, there are significant gaps in information and understanding for coronavirus RTC processing and assembly.

In this study, we determined that the P1-Gln at the nsp13-14 and nsp14-15 cleavage sites are dispensable for recovery and replication in MHV. The resulting viruses were impaired for replication kinetics and had significant fitness disadvantages compared to the wild type (WT). Both mutants had increased mutational frequencies and had altered recombination profiles compared to WT. These data suggest that the MHV RTC can function in alternative conformations, either by incorporation of uncleaved nsp components or through minimal incorporations of cleaved components. A greater understanding of CoV RTC assembly may reveal novel methods for attenuation and therapeutic targets.

RESULTS

Recovery of mutant viruses. To determine the processing requirements for pp1ab nsps12-16 in the betacoronavirus murine hepatitis virus (MHV), we used reverse genetics to

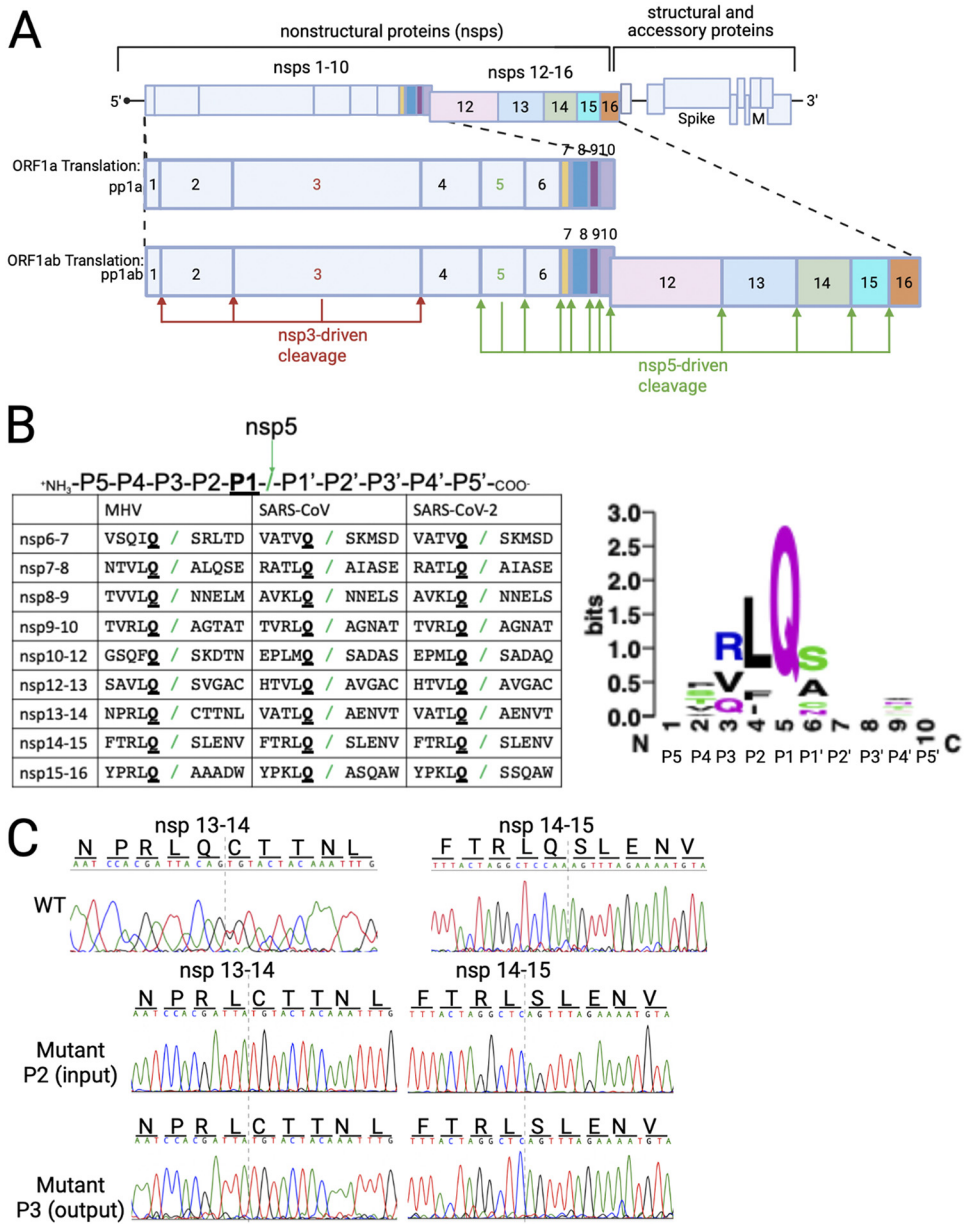

FIG 1 Coronavirus nsp5 cleavage motifs and recovery of nsp13 and nsp14 cleavage mutants. (A) Schematic of MHV genome organization, nonstructural protein expression, and cleavage sites for nsp3 and nsp5 proteases (created with BioRender). (B, left) Alignment of MHV, SARS-CoV, and SARS-CoV-2 nsp5 cleavage motifs for nsps6-16. (Right) Graphical alignment of MHV nsp5 cleavage motifs for nsps6-16; letter size corresponds to sequence conservation. (C) Sanger sequencing traces from DBT-9 cells infected with WT, nsp13-14, or nsp14-15 P2 and P3 stocks. Viral cDNA derived from infected monolayers were Sanger sequenced.

generate in-frame deletions of the nsp5 cleavage site P1-Gln at each subunit interface: nsp12 ΔQ929, nsp13 ΔQ600, nsp14 ΔQ521, and nsp15 ΔQ375. We recovered nsp13 ΔQ600 (nsp13-14) and nsp14 ΔQ521 (nsp14-15) viruses, both of which produced a mixed-plaque phenotype compared to WT MHV that consisted of small- and medium-sized plaques. We did not recover any other mutant, nor was the ΔQ600/ΔQ521 double mutant (nsp13-14-15) recovered. We then generated low-passage stocks of nsp13-14 and nsp14-15 and used the P2 progeny for all experiments presented. The deletions of nsp13-14 nucleotides (18,158-CAG-18,160) and nsp14-15 nucleotides (19,721-CAA-19,723) were confirmed by Sanger sequencing, and after a single round of infection, the resulting P3 progeny maintained the intended deletions during and following infections (Fig. 1C).

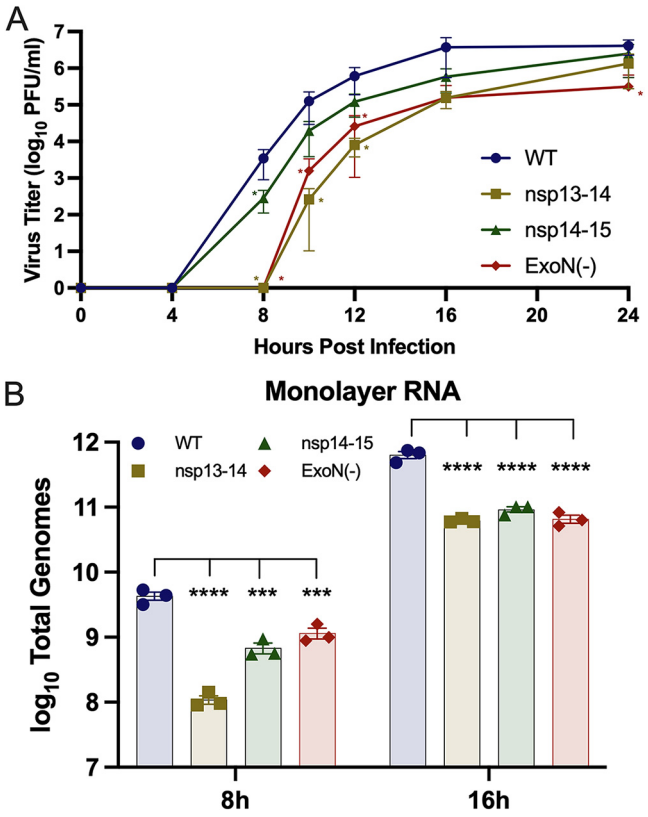

FIG 2 nsp13 and nsp14 cleavage mutants have delayed replication kinetics. (A) DBT-9 cells were infected with MHV WT, nsp13-14, nsp14-15, or ExoN(-) P2 viruses at an MOI of 0.01 PFU/cell. Supernatant samples were collected at the indicated times, and virus titer was determined by plaque assay. Data are means ± standard deviations from three independent experiments. *, $P < 0.05$. All other comparisons were not significant as determined by a one-way ANOVA with Dunnett's multiple-comparison test. (B) DBT-9 cells were infected with the indicated viruses at an MOI of 0.01 PFU/cell. Monolayers were harvested in TRIzol at 8 or 16 h post infection. RNA was purified, and total genomes were quantified by RT-qPCR. Graphed are the individual means from three independent experiments, ± the standard error of the mean (SEM). ***, $P < 0.001$; ****, $P < 0.0001$; ns, not significant (determined by one-way ANOVA with Dunnett's multiple-comparison test).

Replication kinetics of mutant viruses. We first evaluated the impact of the P1-Gln deletions on MHV replication kinetics. Murine astrocytoma DBT-9 cells were infected at a multiplicity of infection (MOI) of 0.01 PFU/cell, and infected cell supernatant samples were collected over 24 h (Fig. 2). Mutant virus replication kinetics were compared to that of both WT MHV and to the well-characterized nsp14 exoribonuclease-inactivating mutant D98A/E91A [ExoN(-)] (45, 47, 48, 53, 65, 66). Infection with the nsp13-14 mutant resulted in a 3 to 10 h delay to exponential phase of replication, while the nsp14-15 virus replication was delayed 1 to 4 h (Fig. 2A). To determine the impact of the P1-Gln deletions on genome production, we performed parallel infections that were harvested at 8 h post infection (hpi) and 16 hpi over three independent experiments. At each time point, the infected monolayers were harvested directly in 1 mL TRIzol reagent for RNA extraction. Monolayer-associated genomes were quantified by 1-step reverse transcription-quantitative PCR (RT-qPCR) with TaqMan probes and primers detecting nsp2 RNA (Fig. 2B). All of the nsp13-14, nsp14-15, and ExoN(-) mutant viruses had reduced RNA production at both time points, consistent with the reductions in titer.

Competitive fitness of mutant viruses. We next evaluated nsp13-14 and nsp14-15 fitness using a coinfection passage competitive fitness assay (66). nsp13-14, nsp14-15, and ExoN(-) viruses were coinfected with WT MHV encoding a genetic barcode of seven silent mutations in the nsp2 coding domain. The infected cell supernatants were

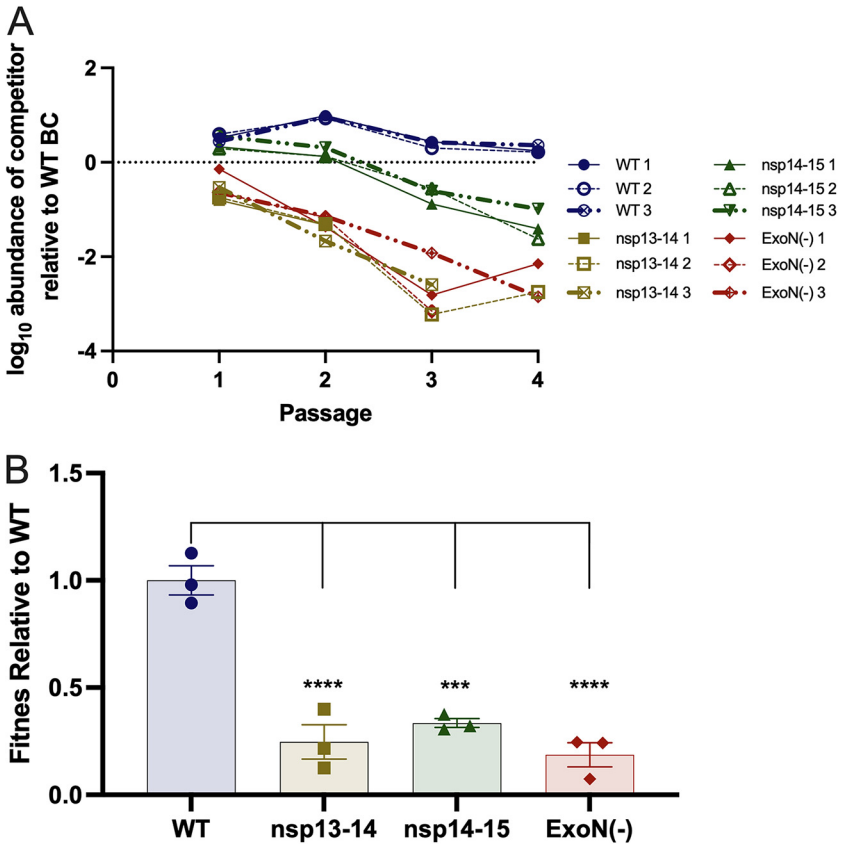

FIG 3 nsp13 and nsp14 cleavage mutants are less fit compared to WT. DBT-9 cells were coinfected with a barcoded (BC) WT MHV and nonbarcoded WT, nsp13-14, nsp14-15, or ExoN(-) at a combined MOI of 0.1 PFU/cell. The resulting supernatants were passaged 3 times. (A) The relative quantities of barcoded and nonbarcoded cDNAs were plotted over passage for the three independent lineages of each competition. (B) Linear regression from panel A was used to determine relative fitness for each nonbarcoded virus. Individual data ($n = 3$) are graphed (means ± SEM). ***, $P < 0.001$; ****, $P < 0.0001$ (determined by one-way ANOVA with Dunnett's multiple-comparison test).

then harvested at 16 h, titers were determined, and supernatants were passaged three additional times. Each passage supernatant was harvested, and RNA was extracted with TRIzol reagent. Primers detecting either the barcoded (WT infection) or nonbarcoded (WT control, mutant competitor) nsp2 cDNA were used in RT-qPCR reactions. The ratio of nonbarcoded to barcoded cDNA was plotted over passage number. All mutant competitor cDNAs were less abundant than WT by passage 2, with a continued downward trend through passage 4 (Fig. 3A). Only nsp13-14 lineage 2 was present during the entire course of the experiment: nsp13-14 lineage 1 was undetectable by passage 3, and lineage 3 was undetectable by passage 4. Similarly, ExoN(-) lineage 2 was not detectable past passage 3. This suggests that these lineages were outcompeted by WT past the limit of detection for this assay. For each viral lineage, linear regression of the plotted ratios over passage was used to determine the relative fitness for each mutant compared to WT (Fig. 3B). Both cleavage mutants and ExoN(-) had significant reductions in fitness relative to WT. These data support the replication kinetics observations and demonstrate that though viable, the P1-Gln deletions conferred significant fitness costs.

Mutation frequencies in mutant viruses. We previously reported that genetic alteration of the nsp14 exonuclease active site and at the interface of nsp10 and nsp14 reduces the replication fidelity of MHV and severe acute respiratory syndrome coronavirus (SARS-CoV) (44, 45, 47, 48). These studies as well as structure and biochemistry results have led to models that nsp14 and its activity is a central regulator of coronavirus

replication fidelity. To determine how the nsp13 and nsp14 P1-Gln deletions affect the replication fidelity of MHV, we analyzed RNA from infected cells 8 h and 16 h post infection by short-read Illumina RNA-sequencing (RNA-seq), and we determined the mutational frequency for each virus at both time points by using the CoVariant pipeline (Fig. 4 and 5) (67). The sequencing depth for all viruses was greater at 16 h than at 8 h (Fig. 4), concomitant with increased genome replication (Fig. 2B). At 8 hpi, there were no statistical differences in the mutational frequencies between WT or any mutant (Fig. 5A). In contrast, the mutation frequency for WT significantly decreased at 16 hpi, but it did not change for the mutants. At 16 hpi, all three mutants had significantly higher mutation frequencies than WT. Because we previously reported that loss of ExoN activity in SARS-CoV resulted in proportionally more transitions than transversions (44), we next asked whether the mutants produced a specific mutational profile during infection by categorizing the sequenced variants as transitions or transversions (Fig. 5B and C; Table 1). Neither cleavage mutant had statistical differences in total transition or transversion frequencies at 8 hpi, while both mutants had significantly higher total transversion frequencies at 16 hpi. ExoN(-) had significantly higher transversion frequencies at both time points and a significantly higher transition frequency at 16 hpi. The individual transition and transversion frequencies are detailed in Table 1, which reveals the unique mutational profile for each cleavage mutant and ExoN(-).

Analysis of nsp13-14 and nsp14-15 recombination. We previously reported that nsp14 enzymatic activity is required for efficient recombination (53). To determine if the nsp13 and nsp14 P1-Gln deletions affect recombination patterns, we analyzed the same RNA-seq data from 8-h and 16-h infected cell monolayers with the RecombiVIR analysis pipeline to quantify and identify all recombination junctions that resulted in defective viral genomes (DVGs) and subgenomic RNAs (sgmRNAs). nsp13-14 had a reduced recombination junction frequency (JFreq; the total number of junction nucleotides per 10^6 mapped nucleotides) at both time points, while nsp14-15 had no statistical differences in JFreq at either time point (Fig. 6A). We next delineated the total number of DVGs and sgmRNA junctions for all viruses at both time points. Both mutants had similar proportions of both total DVGs and sgmRNA junctions at 8 hpi compared to WT, while nsp13-14 had a significantly larger proportion of DVGs at 16 hpi compared to WT, with a concomitant smaller proportion of sgmRNA junctions (Fig. 6B). We further quantified the canonical sgmRNAs for all viruses at each time point (Fig. 6C and D). At 8 hpi, both viruses had changes in sgmRNA 6: nsp13-14 had significantly less, and nsp14-15 had significantly more. However, these changes were not enough to account for a significant change to the total sgmRNA junction type, as shown in Fig. 6B. At 16 hpi, nsp13-14 had significantly fewer junctions for every type of sgmRNA, accounting for the overall change in sgmRNA junctions. nsp14-15 also had changes in sgmRNA junction production; however, some sgmRNA junctions were slightly lower (sgmRNAs 2, 3, and 4) than WT, while sgmRNA 6 was higher than WT. Additionally, we analyzed the recombination patterns for ExoN(-) at both time points, which had more significant changes in DVG and sgmRNA recombination patterns than either nsp13-14 or nsp14-15 (Fig. 6A to D), and these patterns were consistent with a previous report (53).

DISCUSSION

Here, we show that MHV particles can replicate in the absence of P1 Glns between nsp13-14 and nsp14-15. Several structures have been solved for coronavirus replicase proteins. These include structures for the following: nsp12 RdRp and nsp13 Hel alone and in complex with nsp7 and nsp8 (30, 42, 68–75); nsp14 in complex with nsp10 (37, 55–57); nsp16 also in complex with nsp10 (34, 76–79); hexameric nsp15 (80–85); and nsp9 (31, 86, 87). Despite this catalog of structural data, there are no reported solved structures for a complete RTC incorporating nsps7-16 or incorporating more than two enzymatic proteins (nsps 12 and 13). Additionally, there are no reported structures for the pp1a, pp1ab, or processing-intermediate polyproteins. Atomistic models of coronavirus RTCs are beginning

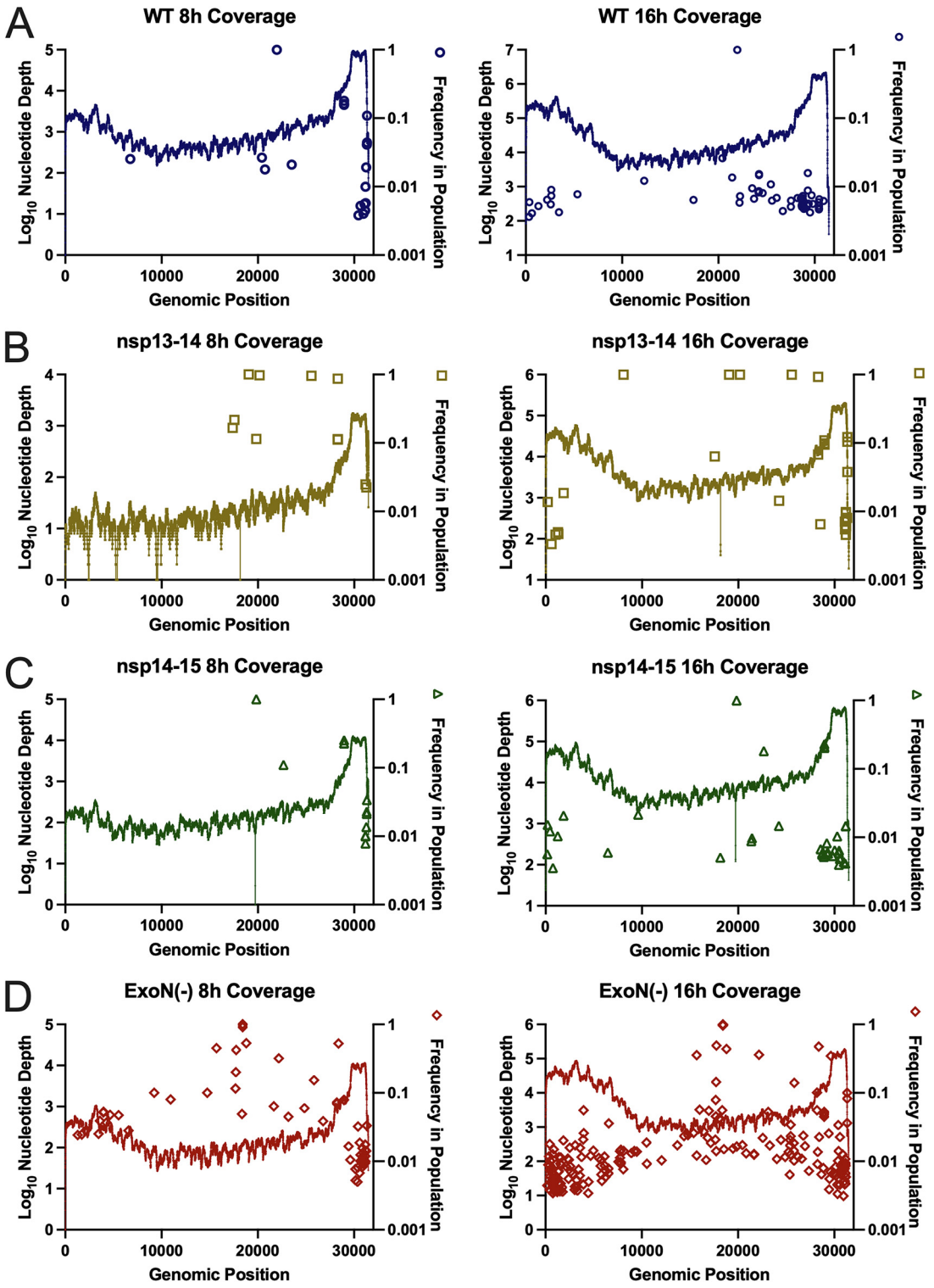

FIG 4 RNA-seq coverage maps and variant locations. DBT-9-infected monolayer RNAs from experiments shown in Fig. 2B were analyzed by RNA-seq for MHV WT (A), nsp13-14 (B), nsp14-15 (C), or ExoN(-) (D) at 8 h and 16 h post infection. Connected lines denote the depth of coverage, corresponding to the left *y* axis, and individual symbols denote the frequencies for the individual variants, corresponding to the right *y* axis, as they relate to the genomic positions. Shown are representative results from one of three independent experiments with similar outcomes.

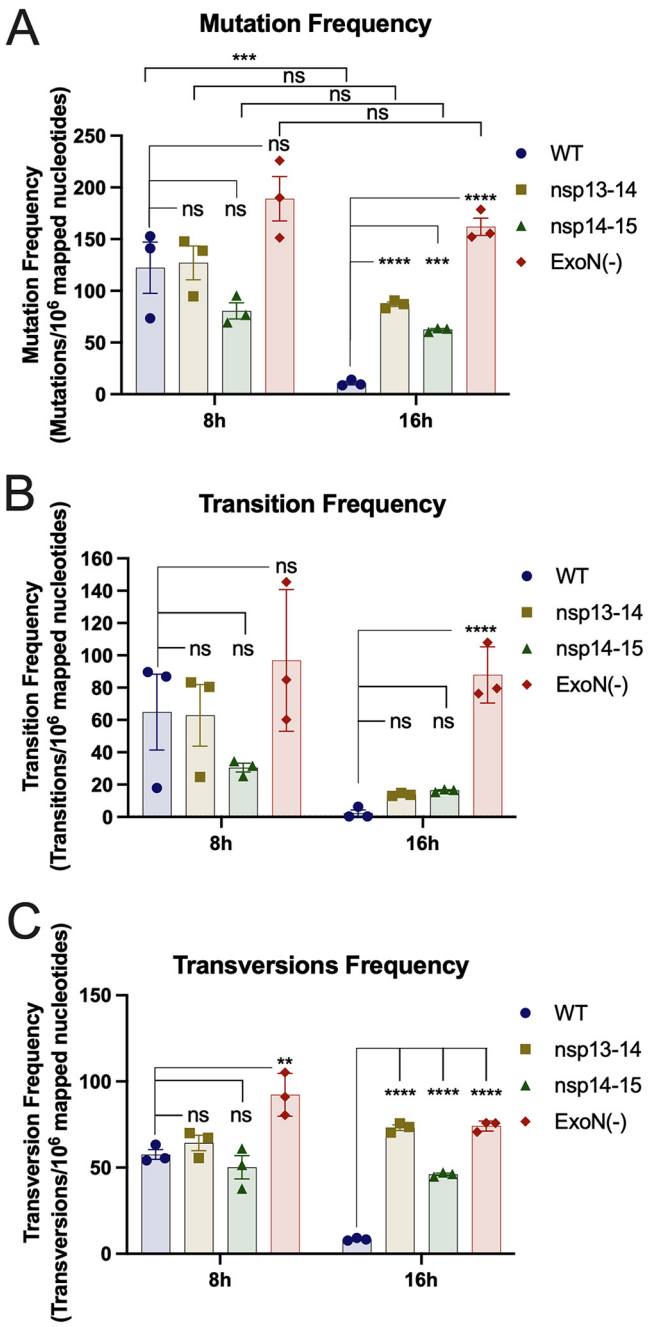

FIG 5 nsp13 and nsp14 cleavage mutants have increased mutation frequencies at late time points during infection. DBT-9-infected monolayer RNAs from experiments shown in Fig. 2B were analyzed by RNA-seq for the indicated viruses, and variant calling was performed on the resulting sequences. Frequencies of mutations (A), transitions (B), and transversions (C) were determined as the ratio of mutations per 1 million mapped nucleotides. Graphed are the individual values (n = 3 independent experiments) ± SEM. ***, $P < 0.001$; ****, $P < 0.0001$; ns, not significant (determined by one-way ANOVA with Dunnett's multiple-comparison test).

to be reported based on available structural data for the various components (88). However, these models only provide possible snapshots for the complete RTC. Additionally, all coronavirus RTC models assume complete maturation of the subunit proteins. Our data challenge this assumption and suggest that the MHV RTC can adopt alternate conformations that either assemble with uncleaved nsp14 intermediates or assemble a minimal component complex that precludes uncleaved subunits, albeit with significant fitness costs (Fig. 3) and impairments to RNA synthesis (Fig. 2B).

TABLE 1 Mutation frequency by mutation type

Type of mutation	Change	Time post infection	Mutation frequency[a]										
			WT		nsp13-14			nsp14-15			ExoN(-)		
			Mean	SEM	Mean	SEM	*P* value	Mean	SEM	*P* value	Mean	SEM	*P* value
Transitions	A to G	8 h	1.391	0.390	0.000	0.000	ns	6.175	0.430	****	8.961	0.371	****
		16 h	0.000	0.000	0.812	0.311	ns	5.507	0.221	****	14.364	0.356	****
	G to A	8 h	13.308	1.452	1.766	1.766	**	18.660	1.342	ns	35.267	2.482	****
		16 h	0.953	0.953	3.831	0.165	*	10.891	0.345	****	31.442	0.461	****
	C to U	8 h	43.997	21.945	59.688	22.205	ns	2.718	1.385	ns	32.218	26.398	ns
		16 h	1.055	1.006	8.546	0.180	ns	0.000	0.000	ns	15.848	9.675	ns
	U to C	8 h	6.143	0.550	1.374	1.374	ns	2.921	0.215	ns	20.380	5.134	*
		16 h	0.304	0.055	0.687	0.006	ns	0.018	0.018	ns	26.261	0.185	****
Transversions	A to U	8 h	16.453	0.466	0.000	0.000	*	5.592	5.592	ns	12.094	2.566	ns
		16 h	3.705	0.146	3.835	0.112	ns	10.853	0.268	****	11.105	0.376	****
	U to A	8 h	15.249	0.488	38.802	3.732	****	19.198	0.663	ns	18.555	0.839	ns
		16 h	0.145	0.023	35.085	0.773	****	12.373	0.287	****	19.460	1.595	****
	A to C	8 h	0.218	0.188	1.668	1.668	ns	0.245	0.245	ns	39.146	0.501	****
		16 h	0.000	0.000	5.228	0.185	****	0.131	0.121	ns	17.567	0.336	****
	C to A	8 h	1.947	1.205	3.273	2.572	ns	0.000	0.000	ns	4.531	2.029	ns
		16 h	2.752	0.358	3.082	0.657	ns	3.922	0.519	ns	6.542	0.491	**
	C to G	8 h	0.000	0.000	0.000	0.000	ns	0.000	0.000	ns	0.364	0.364	ns
		16 h	0.000	0.000	0.000	0.000	ns	0.000	0.000	ns	0.990	0.127	****
	G to C	8 h	0.000	0.000	0.000	0.000	ns	0.000	0.000	ns	0.478	0.048	****
		16 h	0.000	0.000	0.000	0.000	ns	0.000	0.000	ns	1.515	0.324	***
	G to U	8 h	23.712	0.911	3.631	3.631	**	22.511	3.296	ns	16.307	4.087	ns
		16 h	1.398	0.239	12.768	0.320	****	16.739	1.107	****	14.153	0.724	****
	U to G	8 h	0.044	0.044	16.941	1.942	****	2.600	0.516	ns	0.780	0.780	ns
		16 h	0.384	0.116	13.189	0.149	****	2.093	0.363	ns	2.800	0.958	*

[a]DBT-9-infected monolayer RNAs from experiments shown in Fig. 2B were analyzed by RNA-seq for the indicated viruses, and variant calling was performed on the resulting sequences. The mean mutation frequency (the ratio of mutations per 1 million mapped nucleotides) ($n = 3$ independent experiments) for each type of mutation is presented, ± SEM. *, $P < 0.05$; **, $P < 0.01$; ***, $P < 0.001$; ****, $P < 0.0001$; ns, not significant (determined by one-way ANOVA with Dunnett's multiple-comparisons test).

Our RNA-seq experiments revealed that mutation frequency decreases during WT infection. Current models of CoV replication fidelity are based on experiments involving a single time point of infection (44, 45, 47), suggesting that the coronavirus error rate is fixed. Our data suggest that the error rate of the replicase complex may not be fixed but instead may change during infection, either by an unknown activation requirement for nsp14 ExoN or through incorporation of nsp14 and other subunits into the RTC. We hypothesize that the composition of the WT replicase complex is distinct at early and late time points during infection. Early replicase complexes could incorporate fewer components that only include fully processed subunits, or they could include processing intermediates that are cleaved *in situ*. Biochemical experiments indicate that *de novo* RNA synthesis initiation only requires nsps 7, 8, and 12 (29). While these findings have not been translated to viral experiments, they do suggest that a minimal component complex could form during nsp5 processing, allowing genome replication to start.

Unlike WT MHV, the mutation frequencies for nsp13-14, nsp14-15, and ExoN(-) did not decrease over time. Both nsp13-14 and nsp14-15 mutants have intact ExoN DE-E-D motifs, which suggests that the higher mutation frequencies observed with the cleavage mutants were driven by a different mechanism than ExoN(-). This hypothesis is supported by the observed unique mutational profiles of transitions and transversions (Fig. 5B and C; Table 1) and recombination patterns (Fig. 6). Several different mechanisms could explain this observation. The enzymatic activity of the uncleaved nsp14 polyproteins may be sterically hindered by the bulky additions of nsp13 and nsp15, altering or preventing nsp14 incorporation into the RTC. The complex could also suffer from a lack of or misincorporation of the uncleaved nsp13 and nsp15 polyproteins as well, altering the normal functions of both enzymes. Uncleaved nsp13-14 could also impact the interaction of nsp10 with nsp14, as nsp10 interacts with the N-terminal ExoN domain of nsp14 (35–37, 55–57) and stimulates ExoN activity (35, 48).

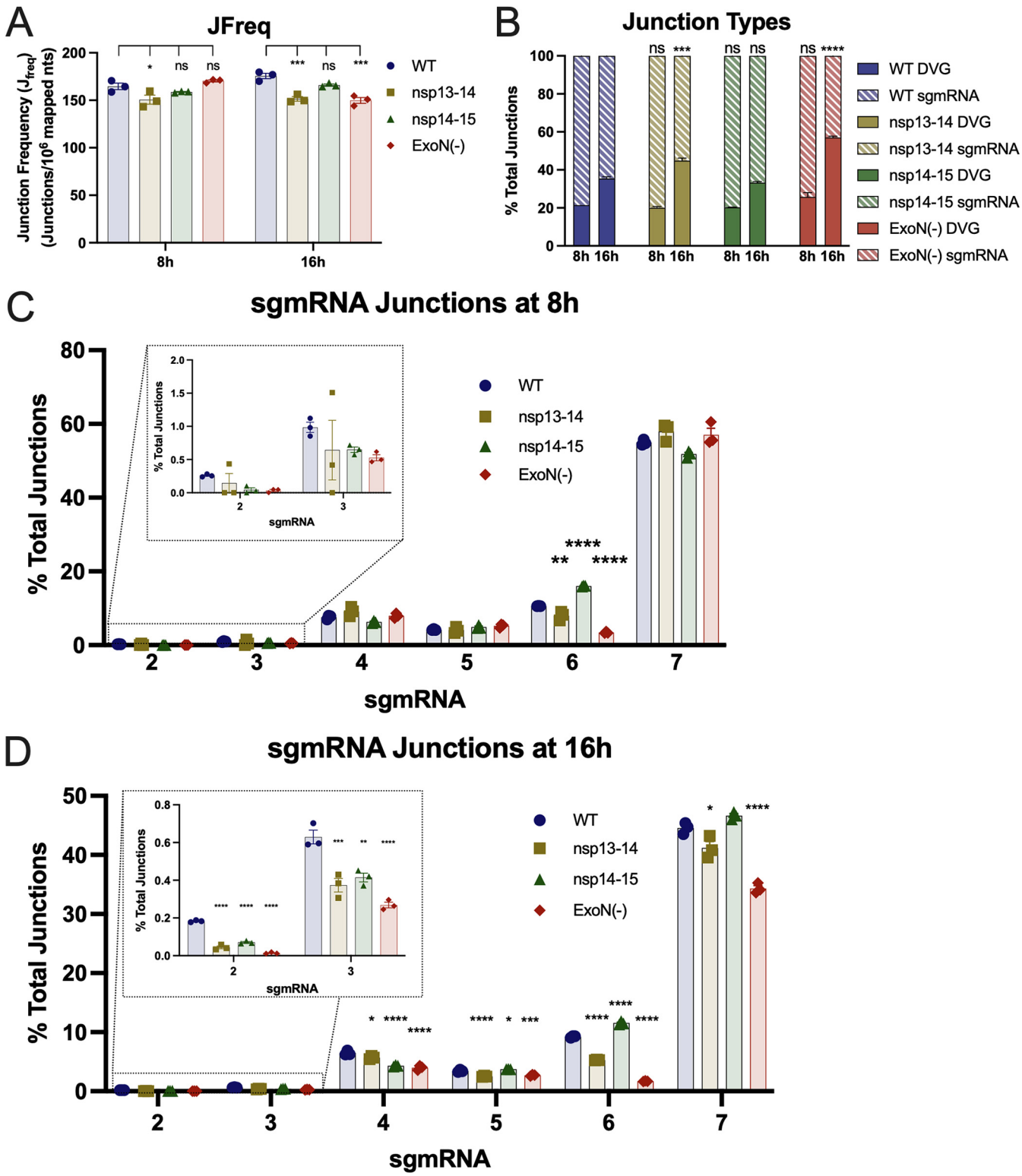

FIG 6 nsp13 and nsp14 cleavage mutants have altered DVG and subgenomic populations. DBT-9-infected monolayer RNAs from experiments shown in Fig. 2B were analyzed by RNA-seq for the indicated viruses, and sequences were aligned to the MHV WT genome using *ViReMa*. (A) The junction frequency (J_{freq}) was calculated as the ratio of detected junctions per 1 million mapped nucleotides. Graphed are the individual values (n = 3 independent experiments) ± SEM. *, $P < 0.05$; ***, $P < 0.001$; ns, not significant (determined by one-way ANOVA with Dunnett's multiple-comparison test). (B) Junction frequencies were calculated for defective viral genomes (DVGs) (solid bars) and total subgenomic RNAs (striped bars) and plotted as percentages of total mapped junctions. Graphed are the mean values (n = 3 independent experiments) ± SEM. ***, $P < 0.001$; ****, $P < 0.0001$; ns, not significant (determined by one-way ANOVA with Dunnett's multiple-comparison test). (C and D) Individual sgmRNA junction frequencies from panel B are shown for the 8-h (C) and 16-h (D) time points. Graphed are the individual values (n = 3 independent experiments) ± SEM. *, $P < 0.05$; **, $P < 0.01$; ***, $P < 0.001$; ****, $P < 0.0001$; all other comparisons were not significant as determined by one-way ANOVA with Dunnett's multiple-comparison test.

While several studies have reported on nsp5 processing and subunit specificity, little is known about the mechanism, timing, and order of pp1a and pp1ab cleavage. Recent biochemical work reported by Krichel et al. proposed a processing order for SARS-CoV nsp7-10 cleavage; however, it is unclear if these data reflect maturation in the broader context of pp1a and pp1ab structure and processing (89). As such, there is currently no model for coronavirus maturation or assembly of the RTC. It is currently unclear how or if the cleavage disruption of nsp13-14 and nsp14-15 would impact the nsp5 processing of other nsps. Without a mechanistic understanding of pp1a and pp1ab cleavage and the order or kinetic rates of the individual cleavage events, this answer is difficult to predict. nsp5 may process the large polyproteins in a linear cleavage order or through processing intermediates, liberating chunks of nsps at a time (90–98). Tertiary and quaternary structures of any resultant processing intermediates may allow nsp5 access to previously inaccessible cleavage motifs. It is also possible that processing intermediates have roles in replication as well, as has been demonstrated for infectious bovine viral diarrhea virus (99) and hypothesized for MHV (23). Disruption of any of the cleavages may prevent further intermediate processing or downstream cleavages or result in alternative cleavage orders (100), causing a stoichiometric imbalance with the processed subunits. The recent structures of SARS-CoV-2 nsp5 in various cleavage states with and without peptidyl substrates are promising advances in understanding the mechanisms of maturation (101).

Testing of cleavage requirements in MHV pp1a nsps7-12 has shown that all cleavage events are required for virus viability except between nsp9 and nsp10 (23). For the distantly related coronavirus infectious bronchitis virus, cleavage between nsp10 and nsp12 was shown to be dispensable for replication (24). Our results presented here suggest that nsp12-13 and nsp15-16 processing must occur and that at least one nsp14 cleavage (N-terminal or C-terminal) must occur to produce viable MHV particles. These results can form the basis for future genetic, structural, and biochemical experiments investigating the mechanisms of coronavirus replicase protein maturation. Ultimately, a greater understanding of coronavirus polyprotein maturation and RTC composition may reveal new targets for therapeutic intervention of current and future coronavirus threats to human health.

MATERIALS AND METHODS

Cell culture. Delayed brain tumor, murine astrocytoma clone 9 (DBT-9) (102) and baby hamster kidney cells stably expressing the MHV receptor (BHK-R) (103) were maintained at 37°C in Dulbecco's modified Eagle's medium containing 4.5 g/liter D-glucose and L-glutamine (DMEM; Gibco) supplemented with 10% FetalClone II serum (FCS; HyClone), 100 U/mL penicillin and streptomycin (Gibco), 10 mM HEPES buffer (Corning), and 0.25 μg/mL amphotericin B (Corning). BHK-R cells were also supplemented with 0.8 mg/mL G418 sulfate (Corning). Cells were routinely washed with Dulbecco's phosphate-buffered saline without calcium chloride or magnesium chloride (PBS −/−). Cells were detached during passage and expansion with 0.05% trypsin-EDTA (Gibco).

Mutagenesis and recovery of viruses. Murine hepatitis virus strain A549 (MHV; GenBank accession number AY910861.1) infectious clones were used as templates for mutagenesis and infection experiments. Site-directed mutagenesis by "round-the-horn" PCR (104) was used to generate in-frame deletions. MHV infectious clone F fragment (103) was used as a template to remove nucleotides 16,358-CAA-16,360 (nsp12 ΔQ929, nsp12-13), 18,158-CAG-18,160 (nsp13 ΔQ600, nsp13-14), 19,721-CAA-19,723 (nsp14 ΔQ521, nsp14-15), and 20,843-CAG-20,845 (nsp15 ΔQ375, nsp15-16) using the following primers: MHV12/13F (5′-AGCGTGGTG CCTGC), MHV12/13R (5′-CAGCACTGCACTTCTTAAATACATGTTCT), MHV13/14F (5′-TGTACTACAAATTTGTTTAA GGATTGTAGCA), MHV13/14R (5′-TAATCGTGGATTGTTAATCTTATCCAACG), MHV14/15F (5′-AGTTTAGAAAATGT AGTGTATAATTTGGTCAATGC), MHV14/15R (5′-GAGCCTAGTAAAAGTATTCCAAAGGTTATAAAAATC), MHV15/16F (5′-GCTGCTGCTGACTGGAAAC), and MHV15/16R (5′-CAAACGAGGATAGAAAGTCATGACCTTC). All primers were 5′-phosphorylated with T4 polynucleotide kinase using an ATP-containing reaction buffer (NEB), and PCRs used Q5 polymerase (NEB). Template backbone DNA was digested with DpnI (NEB), and amplified DNA was separated by electrophoresis and extracted from agarose (Promega). Ligated DNA was transformed into Top10 competent *Escherichia coli* cells (Thermo) and amplified in liquid culture, and sequences were confirmed by Sanger sequencing. Assembly and recovery of recombinant MHV have been described previously (103). Electroporated cells were monitored for cytopathic effect (CPE), and cell flasks were frozen at −80°C when ≈70% of the monolayer was involved in CPE. Cells were thawed, debris was pelleted, and virus-containing supernatants were aliquoted and stored at −80°C (passage 0). Full-genome sequences of the viral mutants were confirmed by Sanger sequencing. Infected cell monolayers were collected in TRIzol (Ambion), and viral RNA was extracted by chloroform extraction and isopropanol precipitation. Viral cDNA was generated with

SuperScript IV reverse transcriptase (Thermo) using random hexamers and oligo(dTs). Three- to 4-kb amplicons were generated via PCR using EasyA polymerase (Agilent) and Sanger sequenced.

Replication and time point experiments. DBT-9 cells were seeded at 6E5 cells in 6-well plates ≈16 h before infection. Cells were infected at an MOI of 0.01 PFU/cell and incubated at 37°C for 1 h. Cells were washed twice in PBS containing calcium chloride or magnesium chloride (PBS +/+), and 3 mL of DMEM was added to each well. At indicated time points, 500 μL of supernatant was collected, and 500 μL of 37°C DMEM was replaced. Supernatant samples were stored at −80°C, and virus titers were determined by plaque assay.

The 8-h and 16-h time course experiments were performed as described above with the following exceptions. Cells for 8-h and 16-h time points were plated in individual wells of a 6-well plate. After inoculation and washing, cells were replaced with 1.5 mL DMEM, and at the indicated time points the entire supernatant was collected, and the monolayer was collected in 1 mL TRIzol. Both supernatant and monolayer samples were stored at −80°C. Supernatant samples were used to determine viral titers and genome quantity (described below), and monolayer samples were used to determine genome quantity and RNA-seq (described below).

Plaque assays and RT-qPCR. Plaque assays were performed in 6-well plates seeded with 6E5 DBT-9 cells. Serial dilutions were plated in duplicate and overlaid with 1% agar in DMEM. Titers were scored at ≈16 h postinfection. Genome quantification was determined by one-step RT-qPCR for supernatant and monolayer-derived RNAs extracted with TRIzol and purified by chloroform and isopropanol precipitation. Viral RNA was detected on a StepOnePlus real-time PCR system (Applied Biosystems) by TaqMan Fast Virus 1-Step Master Mix chemistry (Applied Biosystems) using a 5′ 6-carboxyfluorescein (FAM) and 3′ black hole quencher 1 (BHQ-1)-labeled probe (5′-ATCGCAGGTGTCACCAC) and forward (5′-TGCGGTT TTATCACGCAGTT) and reverse (5′-GGCAACCCACCCACGAA) primers corresponding to nsp2. RNA copy numbers were determine using an nsp2 RNA standard derived from the MHV A fragment.

Competitive fitness experiments. The MHV competitive fitness experiment was previously described in detail (66). Briefly, 1E5 DBT-9 cells were coinfected with the indicated virus and a barcoded (BC) WT MVH reference virus containing seven silent mutations in nsp2 (1301-CAGCAGT-1307) at a total MOI of 0.1 PFU/cell (0.05 MOI for each virus) in three independent lineages. The resulting virus was passaged three additional times, each at a constant MOI of 0.1 PFU/cell. Viral RNA from each passage supernatant was extracted in TRIzol and purified with a KingFisher II (ThermoFisher Scientific) according to the manufacturer's protocol. RNA corresponding to the barcoded WT reference and test viruses was determined by one-step RT-qPCR using SYBR green. BC WT reference RNA was detected with forward (5′-CTATGCTGTATACGGACAGCAGT) and reverse (5′-GGTGTCACCACAACAATCCAC) primers, and test virus RNA was detected with forward (5′-CTATGCTGTATACGGATTCGTCC-3′) reverse (5′-GGTGTCACCACAA CAATCCAC) primers using a Power SYBR green RNA-to-Ct 1-step kit (Applied Biosystems) on a StepOnePlus real-time PCR system (Applied Biosystems). The log-transformed cycle threshold (C_T) ratio of test versus reference was plotted over passage, and relative fitness was determined by comparing the slopes of linear regression.

Short-read Illumina RNA-sequencing of viral RNA. Short-read Illumina RNA-seq libraries were generated from >500 ng of RNA for each sample at the Vantage sequencing core for library preparation (Vanderbilt University Medical Center) and sequenced on the Illumina NovaSeq. Briefly, after quality control, polyadenylated RNA was selected during library preparation. Isolated RNA was heat fragmented, RT-PCR amplified with equivalent number of cycles, and size selected, and libraries were prepared for 2 × 150 nucleotide paired-end sequencing (Illumina). Vantage performed base-calling and read demultiplexing.

Illumina RNA-seq processing and alignment. For recombination analysis, the RecombiVIR pipeline was used (53). The first module of RecombiVIR trims and aligns raw FASTQ files to a viral genome for each sample by using a standard Bash shell script. Similarly, the CoVariant pipeline was used for variant analysis and the first module trims and aligns raw FASTQ files to the viral genome for each specified sample using a standard Bash shell script. To summarize, raw reads were processed by first removing the Illumina TruSeq adapter using Trimmomatic (105). Reads shorter than 36 bp were removed, and low-quality bases (Q score of <30) were trimmed from read ends. The raw FASTQ files were aligned to the MHV-A59 genome (AY910861.1) by using the Python3 script ViReMa (Viral Recombination Mapper, version 0.21) (106) and the command line parameters. For variant analysis, the sequence alignment map (SAM) file was processed using the samtools suite (107), and alignment statistics output was generated by samtools idxstats to an output text file. Nucleotide depth at each position was calculated from the SAM files using BBMap (Bushnell) pileup.sh.

Recombination junction analysis. Following alignment, recombination junctions were filtered, quantified, and annotated by using RecombiVIR_junction_analysis.py with the following command line parameters: python RecombiVIR_junction_anlaysis.py sample.txt MHV ../directory experiment_name - -version 0.21 - -Shannon Entropy ../Shannon_Entropy - -Virus_Accession AY910861.1.

In summary, the recombination J_{freq} was calculated by comparing the number of nucleotides in detected recombination junctions to the total number of mapped nucleotides in a library. J_{freq} was reported as junctions per 10^6 nucleotides sequenced. Mean J_{freq} values were reported.

Identification of sgmRNA and DVG junctions. Forward recombination junctions were classified as either sgmRNA junctions or DVG junctions, based on the position of their junction sites, and filtered in module 2 of RecombiVIR (RecombiVIR_junction_analysis.py). Briefly, junction start sites were filtered to those positioned within 30 nucleotides of the transcriptional regulatory sequence leader (TRS-L) for each virus. The stop sites were then filtered for those positioned within 30 nucleotides of each respective sgmRNA TRS. This window is supported by other reports defining the flexibility of the CoV

transcriptome (108, 109). The J_{freq} of each sgmRNA was calculated by dividing the number of nucleotides in a specific sgmRNA population by the total amount of viral RNA (total mapped nucleotides). This ratio was multiplied by 10^6 to scale for the number of nucleotides sequenced. DVG J_{freq} was calculated by dividing the number of nucleotides in DVG junctions by the total amount of viral RNA in a sample (total mapped nucleotides). The ratio was also multiplied by 10^6 to scale for number of nucleotides sequenced. The percentage of sgmRNA and DVG junctions was calculated by comparing the depth of all filtered sgmRNA or DVG junctions to the sum of all detected forward junctions.

Variant analysis. FASTQ files from RNA-seq experiments were aligned and variants called using the CoVariant pipeline (67). Briefly, the reads were aligned to the viral genome using bowtie2, and variants were called using LoFreq to detect low-frequency variants as previously described (67). Variants were annotated, and overall frequencies of mutations and specific mutation types were reported by the CoVariant module 2.

Statistical analysis. GraphPad Prism, version 9 (La Jolla, CA) was used for all statistical analyses. All tests and sample sizes are listed in the figure legends. Statistical tests for the competitive fitness experiments were performed on normalized data.

Data availability. FASTQ files for the RNA-seq variant and recombination analyses have been deposited in the National Center for Biotechnology Information Sequence Read Archive (NCBISRA) under the accession number PRJNA842027. All code used in this study can be accessed at https://github.com/DenisonLabVU.

ACKNOWLEDGMENTS

We thank Lance Eckerle and Steven Sperry for cloning and recovery of mutant viruses. Jennifer Gribble contributed to this work while at Vanderbilt University Medical Center and is currently affiliated with Integrated DNA Technologies, Coralville, IA, USA. This work was supported by NIH grant AI108197.

REFERENCES

1. Dougherty WG, Semler BL. 1993. Expression of virus-encoded proteinases: functional and structural similarities with cellular enzymes. Microbiol Rev 57:781–822. https://doi.org/10.1128/mr.57.4.781-822.1993.
2. Yost SA, Marcotrigiano J. 2013. Viral precursor polyproteins: keys of regulation from replication to maturation. Curr Opin Virol 3:137–142. https://doi.org/10.1016/j.coviro.2013.03.009.
3. Brierley I, Boursnell ME, Binns MM, Bilimoria B, Blok VC, Brown TD, Inglis SC. 1987. An efficient ribosomal frame-shifting signal in the polymerase-encoding region of the coronavirus IBV. EMBO J 6:3779–3785. https://doi.org/10.1002/j.1460-2075.1987.tb02713.x.
4. Brierley I, Digard P, Inglis SC. 1989. Characterization of an efficient coronavirus ribosomal frameshifting signal: requirement for an RNA pseudoknot. Cell 57:537–547. https://doi.org/10.1016/0092-8674(89)90124-4.
5. Plant EP, Pérez-Alvarado GC, Jacobs JL, Mukhopadhyay B, Hennig M, Dinman JD. 2005. A three-stemmed mRNA pseudoknot in the SARS coronavirus frameshift signal. PLoS Biol 3:e172. https://doi.org/10.1371/journal.pbio.0030172.
6. Kelly JA, Olson AN, Neupane K, Munshi S, San Emeterio J, Pollack L, Woodside MT, Dinman JD. 2020. Structural and functional conservation of the programmed -1 ribosomal frameshift signal of SARS coronavirus 2 (SARS-CoV-2). J Biol Chem 295:10741–10748. https://doi.org/10.1074/jbc.AC120.013449.
7. Ziebuhr J, Snijder EJ, Gorbalenya AE. 2000. Virus-encoded proteinases and proteolytic processing in the Nidovirales. J Gen Virol 81:853–879. https://doi.org/10.1099/0022-1317-81-4-853.
8. Anderson J, Schiffer C, Lee S-K, Swanstrom R. 2009. Viral protease inhibitors. Handb Exp Pharmacol 189:85–110. https://doi.org/10.1007/978-3-540-79086-0_4.
9. Denison MR, Kim JC, Ross T. 1995. Inhibition of coronavirus MHV-A59 replication by proteinase inhibitors, p 391–397. *In* Talbot PJ, Levy GA (ed), Corona- and related viruses: current concepts in molecular biology and pathogenesis. Springer US, Boston, MA.
10. Kim JC, Spence RA, Currier PF, Lu X, Denison MR. 1995. Coronavirus protein processing and RNA synthesis is inhibited by the cysteine proteinase inhibitor E64d. Virology 208:1–8. https://doi.org/10.1006/viro.1995.1123.
11. Abdelnabi R, Foo CS, Jochmans D, Vangeel L, De Jonghe S, Augustijns P, Mols R, Weynand B, Wattanakul T, Hoglund RM, Tarning J, Mowbray CE, Sjö P, Escudié F, Scandale I, Chatelain E, Neyts J. 2022. The oral protease inhibitor (PF-07321332) protects Syrian hamsters against infection with SARS-CoV-2 variants of concern. 1. Nat Commun 13:719. https://doi.org/10.1038/s41467-022-28354-0.
12. Perlman S, Netland J. 2009. Coronaviruses post-SARS: update on replication and pathogenesis. Nat Rev Microbiol 7:439–450. https://doi.org/10.1038/nrmicro2147.
13. Saberi A, Gulyaeva AA, Brubacher JL, Newmark PA, Gorbalenya AE. 2018. A planarian nidovirus expands the limits of RNA genome size. PLoS Pathog 14:e1007314. https://doi.org/10.1371/journal.ppat.1007314.
14. Anand K, Palm GJ, Mesters JR, Siddell SG, Ziebuhr J, Hilgenfeld R. 2002. Structure of coronavirus main proteinase reveals combination of a chymotrypsin fold with an extra alpha-helical domain. EMBO J 21:3213–3224. https://doi.org/10.1093/emboj/cdf327.
15. Anand K, Ziebuhr J, Wadhwani P, Mesters JR, Hilgenfeld R. 2003. Coronavirus main proteinase (3CLpro) structure: basis for design of anti-SARS drugs. Science 300:1763–1767. https://doi.org/10.1126/science.1085658.
16. Hegyi A, Ziebuhr J. 2002. Conservation of substrate specificities among coronavirus main proteases. J Gen Virol 83:595–599. https://doi.org/10.1099/0022-1317-83-3-595.
17. Gao F, Ou H-Y, Chen L-L, Zheng W-X, Zhang C-T. 2003. Prediction of proteinase cleavage sites in polyproteins of coronaviruses and its applications in analyzing SARS-CoV genomes. FEBS Lett 553:451–456. https://doi.org/10.1016/s0014-5793(03)01091-3.
18. Thiel V, Ivanov KA, Putics Á, Hertzig T, Schelle B, Bayer S, Weißbrich B, Snijder EJ, Rabenau H, Doerr HW, Gorbalenya AE, Ziebuhr J. 2003. Mechanisms and enzymes involved in SARS coronavirus genome expression. J Gen Virol 84:2305–2315. https://doi.org/10.1099/vir.0.19424-0.
19. Yang H, Yang M, Ding Y, Liu Y, Lou Z, Zhou Z, Sun L, Mo L, Ye S, Pang H, Gao GF, Anand K, Bartlam M, Hilgenfeld R, Rao Z. 2003. The crystal structures of severe acute respiratory syndrome virus main protease and its complex with an inhibitor. Proc Natl Acad Sci U S A 100:13190–13195. https://doi.org/10.1073/pnas.1835675100.
20. Xue X, Yu H, Yang H, Xue F, Wu Z, Shen W, Li J, Zhou Z, Ding Y, Zhao Q, Zhang XC, Liao M, Bartlam M, Rao Z. 2008. Structures of two coronavirus main proteases: implications for substrate binding and antiviral drug design. J Virol 82:2515–2527. https://doi.org/10.1128/JVI.02114-07.
21. Zhao Q, Li S, Xue F, Zou Y, Chen C, Bartlam M, Rao Z. 2008. Structure of the main protease from a global infectious human coronavirus, HCoV-HKU1. J Virol 82:8647–8655. https://doi.org/10.1128/JVI.00298-08.
22. Woo PCY, Huang Y, Lau SKP, Tsoi H, Yuen K. 2005. In silico analysis of ORF1ab in coronavirus HKU1 genome reveals a unique putative cleavage site of coronavirus HKU1 3C-like protease. Microbiol Immunol 49:899–908. https://doi.org/10.1111/j.1348-0421.2005.tb03681.x.
23. Deming DJ, Graham RL, Denison MR, Baric RS. 2007. Processing of open reading frame 1a replicase proteins nsp7 to nsp10 in murine hepatitis

virus strain A59 replication. J Virol 81:10280–10291. https://doi.org/10.1128/JVI.00017-07.
24. Fang SG, Shen H, Wang J, Tay FPL, Liu DX. 2008. Proteolytic processing of polyproteins 1a and 1ab between non-structural proteins 10 and 11/12 of Coronavirus infectious bronchitis virus is dispensable for viral replication in cultured cells. Virology 379:175–180. https://doi.org/10.1016/j.virol.2008.06.038.
25. Piñón JD, Teng H, Weiss SR. 1999. Further requirements for cleavage by the murine coronavirus 3C-like proteinase: identification of a cleavage site within ORF1b. Virology 263:471–484. https://doi.org/10.1006/viro.1999.9954.
26. Zhai Y, Sun F, Li X, Pang H, Xu X, Bartlam M, Rao Z. 2005. Insights into SARS-CoV transcription and replication from the structure of the nsp7-nsp8 hexadecamer. Nat Struct Mol Biol 12:980–986. https://doi.org/10.1038/nsmb999.
27. Imbert I, Guillemot J-C, Bourhis J-M, Bussetta C, Coutard B, Egloff M-P, Ferron F, Gorbalenya AE, Canard B. 2006. A second, non-canonical RNA-dependent RNA polymerase in SARS coronavirus. EMBO J 25:4933–4942. https://doi.org/10.1038/sj.emboj.7601368.
28. Te Velthuis AJW, van den Worm SHE, Snijder EJ. 2012. The SARS-coronavirus nsp7+nsp8 complex is a unique multimeric RNA polymerase capable of both de novo initiation and primer extension. Nucleic Acids Res 40:1737–1747. https://doi.org/10.1093/nar/gkr893.
29. Subissi L, Posthuma CC, Collet A, Zevenhoven-Dobbe JC, Gorbalenya AE, Decroly E, Snijder EJ, Canard B, Imbert I. 2014. One severe acute respiratory syndrome coronavirus protein complex integrates processive RNA polymerase and exonuclease activities. Proc Natl Acad Sci U S A 111:E3900. https://doi.org/10.1073/pnas.1323705111.
30. Kirchdoerfer RN, Ward AB. 2019. Structure of the SARS-CoV nsp12 polymerase bound to nsp7 and nsp8 co-factors. Nat Commun 10:2342. https://doi.org/10.1038/s41467-019-10280-3.
31. Egloff M-P, Ferron F, Campanacci V, Longhi S, Rancurel C, Dutartre H, Snijder EJ, Gorbalenya AE, Cambillau C, Canard B. 2004. The severe acute respiratory syndrome-coronavirus replicative protein nsp9 is a single-stranded RNA-binding subunit unique in the RNA virus world. Proc Natl Acad Sci U S A 101:3792–3796. https://doi.org/10.1073/pnas.0307877101.
32. Slanina H, Madhugiri R, Bylapudi G, Schultheiß K, Karl N, Gulyaeva A, Gorbalenya AE, Linne U, Ziebuhr J. 2021. Coronavirus replication-transcription complex: vital and selective NMPylation of a conserved site in nsp9 by the NiRAN-RdRp subunit. Proc Natl Acad Sci U S A 118:e2022310118. https://doi.org/10.1073/pnas.2022310118.
33. Donaldson EF, Sims AC, Graham RL, Denison MR, Baric RS. 2007. Murine hepatitis virus replicase protein nsp10 is a critical regulator of viral RNA synthesis. J Virol 81:6356–6368. https://doi.org/10.1128/JVI.02805-06.
34. Decroly E, Debarnot C, Ferron F, Bouvet M, Coutard B, Imbert I, Gluais L, Papageorgiou N, Sharff A, Bricogne G, Ortiz-Lombardia M, Lescar J, Canard B. 2011. Crystal structure and functional analysis of the SARS-coronavirus RNA cap 2′-O-methyltransferase nsp10/nsp16 complex. PLoS Pathog 7:e1002059. https://doi.org/10.1371/journal.ppat.1002059.
35. Bouvet M, Imbert I, Subissi L, Gluais L, Canard B, Decroly E. 2012. RNA 3′-end mismatch excision by the severe acute respiratory syndrome coronavirus nonstructural protein nsp10/nsp14 exoribonuclease complex. Proc Natl Acad Sci U S A 109:9372–9377. https://doi.org/10.1073/pnas.1201130109.
36. Bouvet M, Lugari A, Posthuma CC, Zevenhoven JC, Bernard S, Betzi S, Imbert I, Canard B, Guillemot J-C, Lécine P, Pfefferle S, Drosten C, Snijder EJ, Decroly E, Morelli X. 2014. Coronavirus Nsp10, a critical co-factor for activation of multiple replicative enzymes. J Biol Chem 289:25783–25796. https://doi.org/10.1074/jbc.M114.577353.
37. Ma Y, Wu L, Shaw N, Gao Y, Wang J, Sun Y, Lou Z, Yan L, Zhang R, Rao Z. 2015. Structural basis and functional analysis of the SARS coronavirus nsp14–nsp10 complex. Proc Natl Acad Sci U S A 112:9436–9441. https://doi.org/10.1073/pnas.1508686112.
38. Cheng A, Zhang W, Xie Y, Jiang W, Arnold E, Sarafianos SG, Ding J. 2005. Expression, purification, and characterization of SARS coronavirus RNA polymerase. Virology 335:165–176. https://doi.org/10.1016/j.virol.2005.02.017.
39. Te Velthuis AJW, Arnold JJ, Cameron CE, van den Worm SHE, Snijder EJ. 2010. The RNA polymerase activity of SARS-coronavirus nsp12 is primer dependent. Nucleic Acids Res 38:203–214. https://doi.org/10.1093/nar/gkp904.
40. Ahn D-G, Choi J-K, Taylor DR, Oh J-W. 2012. Biochemical characterization of a recombinant SARS coronavirus nsp12 RNA-dependent RNA polymerase capable of copying viral RNA templates. Arch Virol 157:2095–2104. https://doi.org/10.1007/s00705-012-1404-x.
41. Lehmann KC, Gulyaeva A, Zevenhoven-Dobbe JC, Janssen GMC, Ruben M, Overkleeft HS, van Veelen PA, Samborskiy DV, Kravchenko AA, Leontovich AM, Sidorov IA, Snijder EJ, Posthuma CC, Gorbalenya AE. 2015. Discovery of an essential nucleotidylating activity associated with a newly delineated conserved domain in the RNA polymerase-containing protein of all nidoviruses. Nucleic Acids Res 43:8416–8434. https://doi.org/10.1093/nar/gkv838.
42. Hillen HS, Kokic G, Farnung L, Dienemann C, Tegunov D, Cramer P. 2020. Structure of replicating SARS-CoV-2 polymerase. Nature 584:154–156. https://doi.org/10.1038/s41586-020-2368-8.
43. Snijder EJ, Bredenbeek PJ, Dobbe JC, Thiel V, Ziebuhr J, Poon LLM, Guan Y, Rozanov M, Spaan WJM, Gorbalenya AE. 2003. Unique and conserved features of genome and proteome of SARS-coronavirus, an early split-off from the coronavirus group 2 lineage. J Mol Biol 331:991–1004. https://doi.org/10.1016/S0022-2836(03)00865-9.
44. Eckerle LD, Becker MM, Halpin RA, Li K, Venter E, Lu X, Scherbakova S, Graham RL, Baric RS, Stockwell TB, Spiro DJ, Denison MR. 2010. Infidelity of SARS-CoV Nsp14-exonuclease mutant virus replication is revealed by complete genome sequencing. PLoS Pathog 6:e1000896. https://doi.org/10.1371/journal.ppat.1000896.
45. Eckerle LD, Lu X, Sperry SM, Choi L, Denison MR. 2007. High fidelity of murine hepatitis virus replication is decreased in nsp14 exoribonuclease mutants. J Virol 81:12135–12144. https://doi.org/10.1128/JVI.01296-07.
46. Chen Y, Cai H, Pan J, Xiang N, Tien P, Ahola T, Guo D. 2009. Functional screen reveals SARS coronavirus nonstructural protein nsp14 as a novel cap N7 methyltransferase. Proc Natl Acad Sci U S A 106:3484–3489. https://doi.org/10.1073/pnas.0808790106.
47. Smith EC, Blanc H, Surdel MC, Vignuzzi M, Denison MR. 2013. Coronaviruses lacking exoribonuclease activity are susceptible to lethal mutagenesis: evidence for proofreading and potential therapeutics. PLoS Pathog 9:e1003565. https://doi.org/10.1371/journal.ppat.1003565.
48. Smith EC, Case JB, Blanc H, Isakov O, Shomron N, Vignuzzi M, Denison MR. 2015. Mutations in coronavirus nonstructural protein 10 decrease virus replication fidelity. J Virol 89:6418–6426. https://doi.org/10.1128/JVI.00110-15.
49. Graham RL, Becker MM, Eckerle LD, Bolles M, Denison MR, Baric RS. 2012. A live, impaired-fidelity coronavirus vaccine protects in an aged, immunocompromised mouse model of lethal disease. Nat Med 18:1820–1826. https://doi.org/10.1038/nm.2972.
50. Minskaia E, Hertzig T, Gorbalenya AE, Campanacci V, Cambillau C, Canard B, Ziebuhr J. 2006. Discovery of an RNA virus 3′->5′ exoribonuclease that is critically involved in coronavirus RNA synthesis. Proc Natl Acad Sci U S A 103:5108–5113. https://doi.org/10.1073/pnas.0508200103.
51. Case JB, Ashbrook AW, Dermody TS, Denison MR. 2016. Mutagenesis of S-adenosyl-l-methionine-binding residues in coronavirus nsp14 N7-methyltransferase demonstrates differing requirements for genome translation and resistance to innate immunity. J Virol 90:7248–7256. https://doi.org/10.1128/JVI.00542-16.
52. Case JB, Li Y, Elliott R, Lu X, Graepel KW, Sexton NR, Smith EC, Weiss SR, Denison MR. 2018. Murine hepatitis virus nsp14 exoribonuclease activity is required for resistance to innate immunity. J Virol 92:e01531-17. https://doi.org/10.1128/JVI.01531-17.
53. Gribble J, Stevens LJ, Agostini ML, Anderson-Daniels J, Chappell JD, Lu X, Pruijssers AJ, Routh AL, Denison MR. 2021. The coronavirus proofreading exoribonuclease mediates extensive viral recombination. PLoS Pathog 17:e1009226. https://doi.org/10.1371/journal.ppat.1009226.
54. Ogando NS, Zevenhoven-Dobbe JC, van der Meer Y, Bredenbeek PJ, Posthuma CC, Snijder EJ. 2020. The enzymatic activity of the nsp14 exoribonuclease is critical for replication of MERS-CoV and SARS-CoV-2. J Virol 94:e01246-20. https://doi.org/10.1128/JVI.01246-20.
55. Liu C, Shi W, Becker ST, Schatz DG, Liu B, Yang Y. 2021. Structural basis of mismatch recognition by a SARS-CoV-2 proofreading enzyme. Science 373:1142–1146. https://doi.org/10.1126/science.abi9310.
56. Moeller NH, Shi K, Demir Ö, Belica C, Banerjee S, Yin L, Durfee C, Amaro RE, Aihara H. 2022. Structure and dynamics of SARS-CoV-2 proofreading exoribonuclease ExoN. Proc Natl Acad Sci U S A 119:e2106379119. https://doi.org/10.1073/pnas.2106379119.
57. Ferron F, Subissi L, Silveira De Morais AT, Le NTT, Sevajol M, Gluais L, Decroly E, Vonrhein C, Bricogne G, Canard B, Imbert I. 2018. Structural and molecular basis of mismatch correction and ribavirin excision from coronavirus RNA. Proc Natl Acad Sci U S A 115:E162–E171. https://doi.org/10.1073/pnas.1718806115.

58. Decroly E, Imbert I, Coutard B, Bouvet M, Selisko B, Alvarez K, Gorbalenya AE, Snijder EJ, Canard B. 2008. Coronavirus nonstructural protein 16 is a cap-0 binding enzyme possessing (nucleoside-2′O)-methyltransferase activity. J Virol 82:8071–8084. https://doi.org/10.1128/JVI.00407-08.
59. Seybert A, Hegyi A, Siddell SG, Ziebuhr J. 2000. The human coronavirus 229E superfamily 1 helicase has RNA and DNA duplex-unwinding activities with 5′-to-3′ polarity. RNA 6:1056–1068. https://doi.org/10.1017/s1355838200000728.
60. Ivanov KA, Thiel V, Dobbe JC, van der Meer Y, Snijder EJ, Ziebuhr J. 2004. Multiple enzymatic activities associated with severe acute respiratory syndrome coronavirus helicase. J Virol 78:5619–5632. https://doi.org/10.1128/JVI.78.11.5619-5632.2004.
61. Ivanov KA, Ziebuhr J. 2004. Human coronavirus 229E nonstructural protein 13: characterization of duplex-unwinding, nucleoside triphosphatase, and RNA 5′-triphosphatase activities. J Virol 78:7833–7838. https://doi.org/10.1128/JVI.78.14.7833-7838.2004.
62. Lehmann KC, Snijder EJ, Posthuma CC, Gorbalenya AE. 2015. What we know but do not understand about nidovirus helicases. Virus Res 202:12–32. https://doi.org/10.1016/j.virusres.2014.12.001.
63. Ivanov KA, Hertzig T, Rozanov M, Bayer S, Thiel V, Gorbalenya AE, Ziebuhr J. 2004. Major genetic marker of nidoviruses encodes a replicative endoribonuclease. Proc Natl Acad Sci U S A 101:12694–12699. https://doi.org/10.1073/pnas.0403127101.
64. Hackbart M, Deng X, Baker SC. 2020. Coronavirus endoribonuclease targets viral polyuridine sequences to evade activating host sensors. Proc Natl Acad Sci U S A 117:8094–8103. https://doi.org/10.1073/pnas.1921485117.
65. Graepel KW, Lu X, Case JB, Sexton NR, Smith EC, Denison MR. 2017. Proofreading-deficient coronaviruses adapt for increased fitness over long-term passage without reversion of exoribonuclease-inactivating mutations. mBio 8:e01503-17. https://doi.org/10.1128/mBio.01503-17.
66. Graepel KW, Agostini ML, Lu X, Sexton NR, Denison MR. 2019. Fitness barriers limit reversion of a proofreading-deficient coronavirus. J Virol 93:e00711-19. https://doi.org/10.1128/JVI.00711-19.
67. Agostini ML, Pruijssers AJ, Chappell JD, Gribble J, Lu X, Andres EL, Bluemling GR, Lockwood MA, Sheahan TP, Sims AC, Natchus MG, Saindane M, Kolykhalov AA, Painter GR, Baric RS, Denison MR. 2019. Small-molecule antiviral β-d-N 4-hydroxycytidine inhibits a proofreading-intact coronavirus with a high genetic barrier to resistance. J Virol 93:e01348-19. https://doi.org/10.1128/JVI.01348-19.
68. Yan L, Ge J, Zheng L, Zhang Y, Gao Y, Wang T, Huang Y, Yang Y, Gao S, Li M, Liu Z, Wang H, Li Y, Chen Y, Guddat LW, Wang Q, Rao Z, Lou Z. 2021. Cryo-EM structure of an extended SARS-CoV-2 replication and transcription complex reveals an intermediate state in cap synthesis. Cell 184:184–193.e10. https://doi.org/10.1016/j.cell.2020.11.016.
69. Wang Q, Wu J, Wang H, Gao Y, Liu Q, Mu A, Ji W, Yan L, Zhu Y, Zhu C, Fang X, Yang X, Huang Y, Gao H, Liu F, Ge J, Sun Q, Yang X, Xu W, Liu Z, Yang H, Lou Z, Jiang B, Guddat LW, Gong P, Rao Z. 2020. Structural basis for RNA replication by the SARS-CoV-2 polymerase. Cell 182:417–428.e13. https://doi.org/10.1016/j.cell.2020.05.034.
70. Gao Y, Yan L, Huang Y, Liu F, Zhao Y, Cao L, Wang T, Sun Q, Ming Z, Zhang L, Ge J, Zheng L, Zhang Y, Wang H, Zhu Y, Zhu C, Hu T, Hua T, Zhang B, Yang X, Li J, Yang H, Liu Z, Xu W, Guddat LW, Wang Q, Lou Z, Rao Z. 2020. Structure of the RNA-dependent RNA polymerase from COVID-19 virus. Science 368:779–782. https://doi.org/10.1126/science.abb7498.
71. Peng Q, Peng R, Yuan B, Zhao J, Wang M, Wang X, Wang Q, Sun Y, Fan Z, Qi J, Gao GF, Shi Y. 2020. Structural and biochemical characterization of the nsp12-nsp7-nsp8 core polymerase complex from SARS-CoV-2. Cell Rep 31:107774. https://doi.org/10.1016/j.celrep.2020.107774.
72. Chen J, Malone B, Llewellyn E, Grasso M, Shelton PMM, Olinares PDB, Maruthi K, Eng ET, Vatandaslar H, Chait BT, Kapoor TM, Darst SA, Campbell EA. 2020. Structural basis for helicase-polymerase coupling in the SARS-CoV-2 replication-transcription complex. Cell 182:1560–1573.e13. https://doi.org/10.1016/j.cell.2020.07.033.
73. Hao W, Wojdyla JA, Zhao R, Han R, Das R, Zlatev I, Manoharan M, Wang M, Cui S. 2017. Crystal structure of Middle East respiratory syndrome coronavirus helicase. PLoS Pathog 13:e1006474. https://doi.org/10.1371/journal.ppat.1006474.
74. Jia Z, Yan L, Ren Z, Wu L, Wang J, Guo J, Zheng L, Ming Z, Zhang L, Lou Z, Rao Z. 2019. Delicate structural coordination of the severe acute respiratory syndrome coronavirus Nsp13 upon ATP hydrolysis. Nucleic Acids Res 47:6538–6550. https://doi.org/10.1093/nar/gkz409.
75. Yan L, Zhang Y, Ge J, Zheng L, Gao Y, Wang T, Jia Z, Wang H, Huang Y, Li M, Wang Q, Rao Z, Lou Z. 2020. Architecture of a SARS-CoV-2 mini replication and transcription complex. Nat Commun 11:5874. https://doi.org/10.1038/s41467-020-19770-1.
76. Chen Y, Su C, Ke M, Jin X, Xu L, Zhang Z, Wu A, Sun Y, Yang Z, Tien P, Ahola T, Liang Y, Liu X, Guo D. 2011. Biochemical and structural insights into the mechanisms of SARS coronavirus RNA ribose 2′-O-methylation by nsp16/nsp10 protein complex. PLoS Pathog 7:e1002294. https://doi.org/10.1371/journal.ppat.1002294.
77. Krafcikova P, Silhan J, Nencka R, Boura E. 2020. Structural analysis of the SARS-CoV-2 methyltransferase complex involved in RNA cap creation bound to sinefungin. Nat Commun 11:3717. https://doi.org/10.1038/s41467-020-17495-9.
78. Lin S, Chen H, Ye F, Chen Z, Yang F, Zheng Y, Cao Y, Qiao J, Yang S, Lu G. 2020. Crystal structure of SARS-CoV-2 nsp10/nsp16 2′-O-methylase and its implication on antiviral drug design. Signal Transduct Target Ther 5:131. https://doi.org/10.1038/s41392-020-00241-4.
79. Rosas-Lemus M, Minasov G, Shuvalova L, Inniss NL, Kiryukhina O, Brunzelle J, Satchell KJF. 2020. High-resolution structures of the SARS-CoV-2 2′-O-methyltransferase reveal strategies for structure-based inhibitor design. Sci Signal 13:eabe1202. https://doi.org/10.1126/scisignal.abe1202.
80. Ricagno S, Egloff M-P, Ulferts R, Coutard B, Nurizzo D, Campanacci V, Cambillau C, Ziebuhr J, Canard B. 2006. Crystal structure and mechanistic determinants of SARS coronavirus nonstructural protein 15 define an endoribonuclease family. Proc Natl Acad Sci U S A 103:11892–11897. https://doi.org/10.1073/pnas.0601708103.
81. Joseph JS, Saikatendu KS, Subramanian V, Neuman BW, Buchmeier MJ, Stevens RC, Kuhn P. 2007. Crystal structure of a monomeric form of severe acute respiratory syndrome coronavirus endonuclease nsp15 suggests a role for hexamerization as an allosteric switch. J Virol 81:6700–6708. https://doi.org/10.1128/JVI.02817-06.
82. Bhardwaj K, Palaninathan S, Alcantara JMO, Li Yi L, Guarino L, Sacchettini JC, Kao CC. 2008. Structural and functional analyses of the severe acute respiratory syndrome coronavirus endoribonuclease Nsp15. J Biol Chem 283:3655–3664. https://doi.org/10.1074/jbc.M708375200.
83. Zhang L, Li L, Yan L, Ming Z, Jia Z, Lou Z, Rao Z. 2018. Structural and biochemical characterization of endoribonuclease Nsp15 encoded by Middle East respiratory syndrome coronavirus. J Virol 92:e00893-18. https://doi.org/10.1128/JVI.00893-18.
84. Kim Y, Jedrzejczak R, Maltseva NI, Wilamowski M, Endres M, Godzik A, Michalska K, Joachimiak A. 2020. Crystal structure of Nsp15 endoribonuclease NendoU from SARS-CoV-2. Protein Sci 29:1596–1605. https://doi.org/10.1002/pro.3873.
85. Kim Y, Wower J, Maltseva N, Chang C, Jedrzejczak R, Wilamowski M, Kang S, Nicolaescu V, Randall G, Michalska K, Joachimiak A. 2021. Tipiracil binds to uridine site and inhibits Nsp15 endoribonuclease NendoU from SARS-CoV-2. Commun Biol 4:193. https://doi.org/10.1038/s42003-021-01735-9.
86. Sutton G, Fry E, Carter L, Sainsbury S, Walter T, Nettleship J, Berrow N, Owens R, Gilbert R, Davidson A, Siddell S, Poon LLM, Diprose J, Alderton D, Walsh M, Grimes JM, Stuart DI. 2004. The nsp9 replicase protein of SARS-coronavirus, structure and functional insights. Structure 12:341–353. https://doi.org/10.1016/j.str.2004.01.016.
87. Ponnusamy R, Moll R, Weimar T, Mesters JR, Hilgenfeld R. 2008. Variable oligomerization modes in coronavirus non-structural protein 9. J Mol Biol 383:1081–1096. https://doi.org/10.1016/j.jmb.2008.07.071.
88. Perry JK, Appleby TC, Bilello JP, Feng JY, Schmitz U, Campbell EA. 2021. An atomistic model of the coronavirus replication-transcription complex as a hexamer assembled around nsp15. J Biol Chem 297:101218. https://doi.org/10.1016/j.jbc.2021.101218.
89. Krichel B, Falke S, Hilgenfeld R, Redecke L, Uetrecht C. 2020. Processing of the SARS-CoV pp1a/ab nsp7-10 region. Biochem J 477:1009–1019. https://doi.org/10.1042/BCJ20200029.
90. Gao HQ, Schiller JJ, Baker SC. 1996. Identification of the polymerase polyprotein products p72 and p65 of the murine coronavirus MHV-JHM. Virus Res 45:101–109. https://doi.org/10.1016/s0168-1702(96)01368-8.
91. Schiller JJ, Baker SC. 1998. Maturation of the polymerase polyprotein of the coronavirus MHV strain JHM involves a cascade of proteolytic processing events. Adv Exp Med Biol 440:135–139. https://doi.org/10.1007/978-1-4615-5331-1_18.
92. Xu HY, Lim KP, Shen S, Liu DX. 2001. Further identification and characterization of novel intermediate and mature cleavage products released from the ORF 1b region of the avian coronavirus infectious bronchitis virus 1a/1b polyprotein. Virology 288:212–222. https://doi.org/10.1006/viro.2001.1098.

93. Sparks JS, Donaldson EF, Lu X, Baric RS, Denison MR. 2008. A novel mutation in murine hepatitis virus nsp5, the viral 3C-like proteinase, causes temperature-sensitive defects in viral growth and protein processing. J Virol 82:5999–6008. https://doi.org/10.1128/JVI.00203-08.
94. Stobart CC, Lee AS, Lu X, Denison MR. 2012. Temperature-sensitive mutants and revertants in the coronavirus nonstructural protein 5 protease (3CLpro) define residues involved in long-distance communication and regulation of protease activity. J Virol 86:4801–4810. https://doi.org/10.1128/JVI.06754-11.
95. Sawicki SG, Sawicki DL, Younker D, Meyer Y, Thiel V, Stokes H, Siddell SG. 2005. Functional and genetic analysis of coronavirus replicase-transcriptase proteins. PLoS Pathog 1:e39. https://doi.org/10.1371/journal.ppat.0010039.
96. Schiller JJ, Kanjanahaluethai A, Baker SC. 1998. Processing of the coronavirus MHV-JHM polymerase polyprotein: identification of precursors and proteolytic products spanning 400 kilodaltons of ORF1a. Virology 242:288–302. https://doi.org/10.1006/viro.1997.9010.
97. Denison MR, Perlman S. 1986. Translation and processing of mouse hepatitis virus virion RNA in a cell-free system. J Virol 60:12–18. https://doi.org/10.1128/JVI.60.1.12-18.1986.
98. Denison MR, Zoltick PW, Hughes SA, Giangreco B, Olson AL, Perlman S, Leibowitz JL, Weiss SR. 1992. Intracellular processing of the N-terminal ORF 1a proteins of the coronavirus MHV-A59 requires multiple proteolytic events. Virology 189:274–284. https://doi.org/10.1016/0042-6822(92)90703-r.
99. Agapov EV, Murray CL, Frolov I, Qu L, Myers TM, Rice CM. 2004. Uncleaved NS2-3 is required for production of infectious bovine viral diarrhea virus. J Virol 78:2414–2425. https://doi.org/10.1128/jvi.78.5.2414-2425.2004.
100. Wassenaar AL, Spaan WJ, Gorbalenya AE, Snijder EJ. 1997. Alternative proteolytic processing of the arterivirus replicase ORF1a polyprotein: evidence that NSP2 acts as a cofactor for the NSP4 serine protease. J Virol 71:9313–9322. https://doi.org/10.1128/JVI.71.12.9313-9322.1997.
101. Zhao Y, Zhu Y, Liu X, Jin Z, Duan Y, Zhang Q, Wu C, Feng L, Du X, Zhao J, Shao M, Zhang B, Yang X, Wu L, Ji X, Guddat LW, Yang K, Rao Z, Yang H. 2022. Structural basis for replicase polyprotein cleavage and substrate specificity of main protease from SARS-CoV-2. Proc Natl Acad Sci U S A 119:e2117142119. https://doi.org/10.1073/pnas.2117142119.
102. Chen W, Baric RS. 1996. Molecular anatomy of mouse hepatitis virus persistence: coevolution of increased host cell resistance and virus virulence. J Virol 70:3947–3960. https://doi.org/10.1128/JVI.70.6.3947-3960.1996.
103. Yount B, Denison MR, Weiss SR, Baric RS. 2002. Systematic assembly of a full-length infectious cDNA of mouse hepatitis virus strain A59. J Virol 76:11065–11078. https://doi.org/10.1128/jvi.76.21.11065-11078.2002.
104. Ho SN, Hunt HD, Horton RM, Pullen JK, Pease LR. 1989. Site-directed mutagenesis by overlap extension using the polymerase chain reaction. Gene 77:51–59. https://doi.org/10.1016/0378-1119(89)90358-2.
105. Bolger AM, Lohse M, Usadel B. 2014. Trimmomatic: a flexible trimmer for Illumina sequence data. Bioinformatics 30:2114–2120. https://doi.org/10.1093/bioinformatics/btu170.
106. Routh A, Johnson JE. 2014. Discovery of functional genomic motifs in viruses with ViReMa, a virus recombination mapper for analysis of next-generation sequencing data. Nucleic Acids Res 42:e11. https://doi.org/10.1093/nar/gkt916.
107. Li H, Handsaker B, Wysoker A, Fennell T, Ruan J, Homer N, Marth G, Abecasis G, Durbin R, 1000 Genome Project Data Processing Subgroup. 2009. The sequence alignment/map format and SAMtools. Bioinformatics 25:2078–2079. https://doi.org/10.1093/bioinformatics/btp352.
108. Irigoyen N, Firth AE, Jones JD, Chung BY-W, Siddell SG, Brierley I. 2016. High-resolution analysis of coronavirus gene expression by RNA sequencing and ribosome profiling. PLoS Pathog 12:e1005473. https://doi.org/10.1371/journal.ppat.1005473.
109. Kim D, Lee J-Y, Yang J-S, Kim JW, Kim VN, Chang H. 2020. The architecture of SARS-CoV-2 transcriptome. Cell 181:914–921.e10. https://doi.org/10.1016/j.cell.2020.04.011.